Check for updates

Research Article | Vol. 33, No. 6 / 24 Mar 2025 / Optics Express 13217

Optics EXPRESS

Quantum efficiency enhancement using photon-trapping structure on extended SWIR type-II superlattice nBn photodetector

DONGHO GWAK,[1] SEUNG-YEOP AHN,[1] JINHA LIM,[1] JAEYONG JEONG,[1] BYOUNGWOOK LEE,[2] YOUNGHO KIM,[2] AND SANGHYEON KIM[1,*]

[1] *School of Electrical Engineering, Korea Advanced Institute of Science and Technology (KAIST), Daejeon 34141, Republic of Korea*
[2] *i3system, Inc., Daejeon 34113, Republic of Korea*
[*] *shkim.ee@kaist.ac.kr*

Abstract: Type-II superlattice (T2SL) material systems are emerging as promising alternatives to conventional materials such as InGaAs and HgCdTe for extended short-wavelength infrared (eSWIR) detection, a field experiencing growing demand due to its diverse applications. However, T2SL photodetectors typically suffer from relatively low quantum efficiency. In this study, we demonstrate a significant enhancement in the quantum efficiency of eSWIR T2SL photodetectors through the implementation of a photon-trapping structure. The photon-trapping structure, consisting of top diffraction gratings and a bottom reflective metal layer incorporated via wafer bonding, effectively increases the optical path length within the active region by redirecting incident light to propagate laterally. Optical measurements demonstrate a 77.2% improvement in average quantum efficiency for the photon-trapping photodetector compared to a conventional reference photodetector over the 1.7 µm to 2.5 µm wavelength range. Finite-difference time-domain (FDTD) simulations of electric field distributions and optical resonance analyses reveal that this enhancement is driven by the combined effects of Fabry-Perot resonances and multiple guided-mode resonances, arising from the synergy between the bottom reflective metal and the diffraction grating.

© 2025 Optica Publishing Group under the terms of the Optica Open Access Publishing Agreement

1. Introduction

The extended short wavelength infrared (eSWIR) region, spanning from 1.7 to 2.5 µm, is gaining significant attention due to its diverse applications in both civilian and military domains, including surveillance, hyperspectral imaging, astronomical observation, and weather forecasting [1–5]. The two most commonly utilized material systems for eSWIR photodetectors are indium gallium arsenide (InGaAs) and mercury cadmium telluride (HgCdTe, also known as MCT) [6]. However, both materials exhibit inherent limitations that constrain their performance and applicability.

$In_xGa_{1-x}As$ photodetectors, lattice-matched to an indium phosphide (InP) substrate, contain a 53% indium composition, resulting in a cut-off wavelength of 1.7 µm [5,7]. Extending the absorption range of InGaAs towards 2.5 µm necessitates an increase in the indium content. However, this adjustment leads to lattice mismatch with the InP substrate, causing dislocations that degrade the crystallinity of InGaAs, and consequently, impair its performance [8,9]. Furthermore, it significantly impacts the uniformity and structural point defects, imposing challenges in array formation. Meanwhile, the complex growth processes and low yield associated with HgCdTe photodetectors further limit their widespread adoption [10–12].

As an alternative, type-II superlattices (T2SL) have emerged as a promising breakthrough for eSWIR photodetectors. These superlattices offer several advantages, including cost-effectiveness, uniformity, stability in large-area fabrication, and suppression of Auger recombination [11,12].

#554906 https://doi.org/10.1364/OE.554906
Journal © 2025 Received 6 Jan 2025; revised 4 Mar 2025; accepted 5 Mar 2025; published 13 Mar 2025

Optics EXPRESS

A key feature of type-II superlattices is the ability to engineer the band gap by varying material composition and proportions, allowing for the precise tuning of the desired absorption wavelength band [13]. Despite these advantages, type-II superlattices currently suffer from relatively low quantum efficiency compared to other material systems [12,14]. Quantum efficiency, defined as the proportion of incident photons that are converted into photogenerated electrons, is a critical parameter in evaluating photodetector performance [15].

One straightforward approach to enhance quantum efficiency is to increase the thickness of the absorption layer, which extends the optical path length and thereby increases the absorption rate in accordance with the Beer-Lambert law [16]. However, thickening the absorption layer introduces several drawbacks. Firstly, it leads to an increase in dark current, making high-temperature operation difficult [17]. Additionally, thicker absorption layers result in longer epitaxial growth times and higher costs. Furthermore, the absorber layer thickness is limited by the carrier diffusion length, beyond which carrier recombination reduces efficiency [18]. Therefore, it is crucial to increase the effective optical path without compromising the absorber thickness.

An alternative approach to enhancing the quantum efficiency of photodetectors involves coating the device with a thin-film anti-reflection layer to reduce surface reflections. Anti-reflection coatings typically consist of one or more layers of dielectric materials with carefully optimized refractive indices and thicknesses. When incident light interacts with these layers, destructive interference occurs at the interfaces, effectively canceling a portion of the reflected light and thereby reducing overall reflectance. However, anti-reflection coatings have a limitation that they do not prevent light from escaping through the bottom of the active region, which can contribute to optical losses. Additionally, anti-reflection coatings are typically designed for specific wavelengths and incidence angles, making them less effective for broadband imaging and multi-angle applications.

To overcome the limitations of such approaches, photon-trapping has emerged as a pivotal mechanism in the development of advanced infrared photodetectors. The concept of photon-trapping leverages engineered nanostructures to manipulate incident light, creating optical resonances that confine photons within the active region of the detector. Conventional photon-trapping photodetectors typically employ nanostructures such as gratings on the device surface to enhance absorption [4,19–24]. However, these designs suffer from a critical limitation that the absorption layer is placed on substrates with similar refractive indices or on oxides with minimal refractive index contrast. As a result, diffracted light from the upper surface can easily escape through the bottom of the device, making it difficult to form optical resonances and thereby reducing the overall trapping efficiency.

To address these limitations of conventional photon-trapping structures, we introduce a novel approach to enhance the quantum efficiency of infrared photodetectors by integrating a diffraction grating on the upper surface and a reflective metal layer beneath the active region. This configuration completely blocks light from escaping through the bottom of the device, instead reflecting it back into the active layer to facilitate strong Fabry-Perot resonances and guided-mode resonances. We experimentally demonstrate an InAs/GaSb/AlSb/GaSb type-II superlattice n-type/barrier/n-type (nBn) photodetector with significantly enhanced quantum efficiency in the extended short-wavelength infrared range. Employing two-dimensional diffraction gratings on the top surface and a bottom reflective metal layer implemented through wafer bonding, this design enables incident light to be diffracted and propagate laterally along the active layer. As a result, the effective optical path length is elongated without increasing the absorption layer thickness, leading to a substantial improvement in quantum efficiency.

2. Design

Figure 1(a) illustrates the overall structure of the fabricated InAs/GaSb/AlSb/GaSb type-II superlattice photodetector. The epitaxial layers of the type-II superlattice nBn structure consist of the

following layers: a 100 nm InAsSb etch stop layer, a 100 nm n-type InAs/GaSb/AlSb/GaSb 5/1/5/1 monolayer (ML) contact layer, a 1,000 nm InAs/GaSb/AlSb/GaSb 9/1/5/1 ML absorber layer, a 500 nm AlAsSb/GaSb 5/2 ML barrier layer, and another 50 nm n-type InAs/GaSb/AlSb/GaSb 5/1/5/1 ML contact layer. The epitaxial layer structure of this device consists of an n-type absorber and an n-type contact surrounding a barrier layer, forming an nBn architecture. Figure 1(b) presents the band diagram of the nBn structure under reverse bias, where the device operates, illustrating its role in suppressing dark current. In this configuration, the barrier effectively blocks the transport of non-photo-generated electrons outside the absorber region, thereby reducing dark current while allowing efficient photocarrier collection.

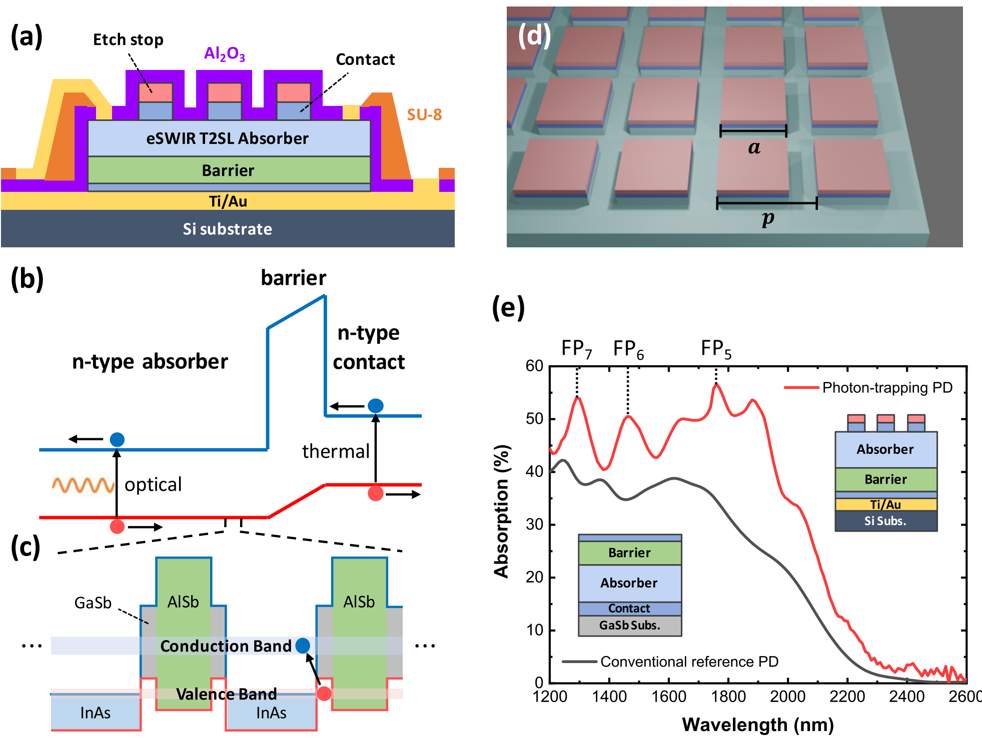

Fig. 1. (a) Structure of the photon-trapping T2SL photodetector. (b) Band diagram of nBn structure under reverse bias. (c) Bandgap alignment of InAs/GaSb/AlSb/GaSb 9/1/5/1 T2SL absorber layer. (d) Schematic of the simulated diffraction gratings. (e) Simulated absorption spectra comparison between conventional reference photodetector with a bare surface and photon-trapping photodetector. The inset shows the schematics of two photodetectors.

Figure 1(c) depicts the bandgap alignment of the T2SL InAs/GaSb/AlSb/GaSb 9/1/5/1 structure consisting absorber layer. The eSWIR T2SL absorber is formed by the periodic growth of these compound layers at specific monolayer thickness ratios, creating the proper bandgap characteristics necessary for optimal infrared detection. Then, the device is fabricated as a mesa structure positioned on a reflective gold layer and passivated with aluminum oxide and SU-8 to mitigate sidewall leakage currents.

To investigate the grating dimensions for enhanced quantum efficiency, finite-difference time-domain (FDTD) simulations were performed using ANSYS Lumerical FDTD. The imaginary index of the eSWIR T2SL absorber was derived using the Beer-Lambert law from the experimentally measured quantum efficiency of the conventional reference photodetector with a bare surface.

Figure 1(d) presents a schematic representation of the diffraction gratings on the active region. Since one-dimensional gratings are sensitive to the polarization of incident light, two-dimensional square-shaped diffraction gratings were chosen to mitigate this effect [25]. The design of the diffraction gratings involves three key parameters: the grating period p, the duty cycle a/p, and the grating height h. By varying these parameters, we calculated the average absorption across the extended short-wavelength infrared region. During the optimization process, we incorporated the slanted grating sidewall profile observed in scanning electron microscope (SEM) imaging to ensure the simulation accurately represents the actual structure. The grating dimensions were determined to be a period of 1.75 µm, a grating size of 1.25 µm, and a grating height of 400 nm based on fabrication feasibility.

Figure 1(e) compares the simulated absorption spectra of the conventional reference photodetector and the photon-trapping photodetector. The conventional reference photodetector exhibited an average absorption of 21.9% across the wavelength range of 1,200 nm to 2,600 nm. In contrast, the photon-trapping photodetector achieved an average absorption of 31.6% over the same range, representing a 44.3% increase. The distinct Fabry-Perot resonances with orders of 5, 6, and 7 induced by the bottom reflective metal are observed at wavelengths of 1.77 µm, 1.48 µm, and 1.27 µm, respectively. The increased absorption in the eSWIR region, in addition to the Fabry-Perot resonances, is attributed to the various guided modes enabled by the photon-trapping structure. For instance, the increased absorption near the fifth Fabry-Perot resonance peak in the eSWIR region is attributed to the optical path elongation facilitated by the combined effects of the diffraction grating and the bottom reflector. In a conventional structure, the incident light passes through the absorber, and any unabsorbed light escapes into the substrate. As a result, the optical path length is limited to the thickness of the absorber. However, in the photon-trapping structure, the diffraction grating scatters the incident light, while the bottom reflective metal prevents it from escaping to the substrate. This configuration allows the light to propagate multiple times through the active region, dramatically elongating the optical path length and ensuring that a greater portion of photons is absorbed by the absorber.

3. Experiment

The type-II superlattice epitaxial layers were grown on a lattice-matched GaSb substrate using molecular beam epitaxy (MBE). If the GaSb substrate directly adjoins the active region, the diffracted incident light may escape from the active region at the interface due to the higher refractive index of GaSb compared to the active region. To ensure that the light travels laterally through the active region, it is necessary to place a reflective metal layer at the bottom of the active region to eliminate transmission out of the active region. This was accomplished using wafer bonding technology [26].

To incorporate the reflective metal beneath the active region, a bare Si substrate was utilized, and 30 nm/100 nm of Ti/Au was deposited onto both the Si substrate and the T2SL epitaxy. The T2SL epitaxy was then flipped and directly bonded with the Si substrate. Here, since the T2SL epitaxy is flipped and bonded, the Ti adhesion layer for the Au reflector is positioned directly beneath the active region. As a result, light passes through the Ti layer before being reflected by the Au reflector, leading to inevitable optical loss due to absorption in the Ti layer. Following the bonding, the GaSb donor substrate was removed via a back etching process using a CrO_3-HF-H_2O solution.

After the removal of the GaSb substrate, optimized diffraction gratings were patterned on the etch stop layer using maskless photolithography with SS03A9 photoresist. The gratings were formed through a wet-etching process employing an H_2O_2-H_3PO_4-$C_6H_8O_7$ mixture. Following the grating formation, the photodetector mesa was defined using the same wet etchant. The defined pixel size was 300×300 µm^2. Immediately after mesa definition and photoresist stripping, the pixels were passivated with a 50 nm thick Al_2O_3 layer using atomic layer deposition

(ALD) to prevent degradation due to surface oxidation. SU-8 was then applied to smooth the sidewalls, ensuring a reliable electrical connection between the top electrode and the contact pad. Subsequently, a contact via was etched into the passivation layer using buffered oxide etchant. Finally, 30 nm/150 nm of Ti/Au was deposited by e-beam evaporation, followed by a lift-off process to form the contacts.

An optical microscope (OM) image of the fabricated photon-trapping photodetector is shown in Fig. 2(a), and an enlarged scanning electron microscope image of the diffraction grating on the device's top surface is presented in Fig. 2(b). The designed dimensions were well-represented by the fabrication process.

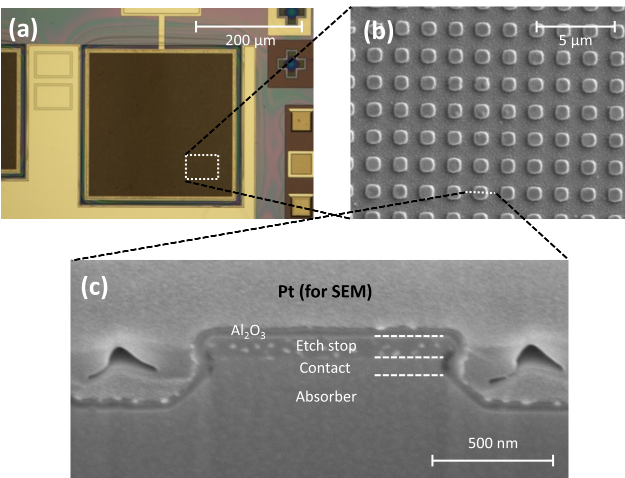

Fig. 2. (a) Optical microscope image of the fabricated photon-trapping photodetector. (b) Scanning electron microscope image of the magnified diffraction gratings on the top surface. (c) Cross-sectional SEM image of the single diffraction grating.

To verify the successful formation of the grating, the cross-sectional profile was examined using focused ion beam (FIB) milling followed by SEM imaging. As shown in Fig. 2(c), the grating structure consists of the etch stop layer, the contact layer, and a part of the absorber, all passivated with Al_2O_3. The background platinum layer was deposited during the FIB milling process to facilitate SEM imaging. The grating height measured via SEM was 395 nm, consistent with the intended design. Due to the inherent limitations of wet etching, the grating sidewalls exhibited a slight slant. A precise dry etching process would likely yield a more vertical grating profile.

4. Results and discussion

Figure 3(a) shows the dark current density as a function of applied bias voltage for the photodetector with a photon-trapping structure, measured at various temperatures ranging from 160 K to 300 K with 20 K interval. At forward bias, the dark current is effectively suppressed due to the barrier that impedes electron flow. The measured dark current density at 160 K under a -0.2 V bias was 4.8×10^{-8} A/cm^2. At room temperature (300 K), the photodetector exhibited a dark current density of 8.6×10^{-3} A/cm^2 under the same bias condition. In comparison to previous studies on eSWIR T2SL photodetectors, the dark current densities of the photon-trapping photodetector were similar or up to five times lower than those reported in other works [27–30].

To determine the activation energy of the device, an Arrhenius plot of the dark current density versus the inverse of temperature (1/T) was generated at -0.2 V bias as shown in Fig. 3(b). A -0.2 V bias was selected since the dark current reaches saturation at this applied bias. Fitting

Optics EXPRESS

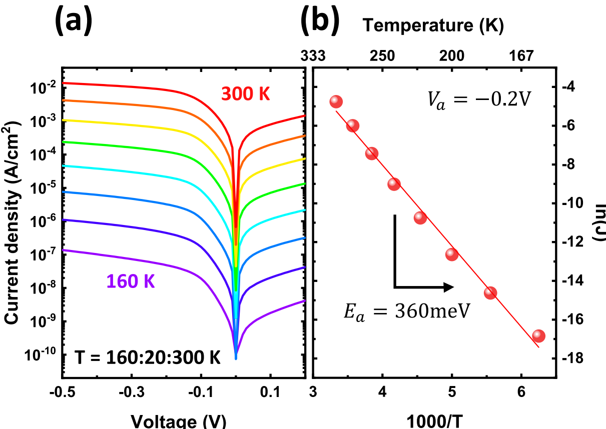

Fig. 3. (a) Dark current density versus applied bias voltage characteristics of photon-trapping photodetector measured at different temperatures. (b) Arrhenius plot of the dark current density under -0.2 V applied bias.

the data from 160 K to 300 K to the Arrhenius equation yielded an activation energy of 360 meV. According to the following analysis of bandgap energy extraction, the activation energy typically lies within the range of half the bandgap energy to the full bandgap energy. In a diffusion-limited photodetector, the activation energy would be expected to match the full bandgap energy. However, the observed discrepancy suggests that additional dark current mechanisms such as generation-recombination processes or trap-assisted tunneling, may be contributing to the overall dark current [31]. This indicates the potential for further dark current reduction by implementing strategies to suppress these non-ideal carrier pathways.

Figure 4 presents the spectral quantum efficiency, which was derived from the spectral responsivity measurements taken under a -0.5 V applied bias across a temperature spanning from 100 K to 300 K with 20 K interval. As the applied bias was gradually increased, the quantum efficiency saturated at -0.5 V, indicating that all photo-generated carriers were fully collected. Therefore, the quantum efficiency spectra were measured at this bias. The overall quantum efficiency increases from 100 K, reaching a peak at 180 K, before declining with further temperature increases. It is believed that this trend is driven by the temperature-dependent behavior of carrier mobility and carrier lifetime [32]. The data exhibit a distinct redshift in the cut-off wavelength as the temperature increases. This shift can be attributed to bandgap narrowing, which occurs due to the thermal expansion of atomic spacing and the enhanced interactions between lattice phonons and electrons at elevated temperatures [33]. From the cut-off wavelengths, we calculated the bandgap energies at various temperatures as shown in the inset of Fig. 4. To estimate the 0 K bandgap energy, we employed the Varshni expression, which is a second-order approximation of the Bose-Einstein model that effectively describes the temperature-dependent changes in bandgap energy [34]. The Varshni expression is given by

$$E_g(T) = E_g(0) - \frac{\alpha T^2}{T + \beta} \tag{1}$$

where $E_g(T)$ is bandgap energy at temperature T; α and β are fitting parameters. By fitting the data with the Varshni expression, the bandgap energy at 0 K was determined to be 576 meV, while the parameters α and β were calculated to be 0.29 meV/K and 107 K, respectively.

To evaluate the quantum efficiency enhancement effect of the photon-trapping photodetector, we fabricated and measured the quantum efficiencies of two additional reference photodetectors.

Optics EXPRESS

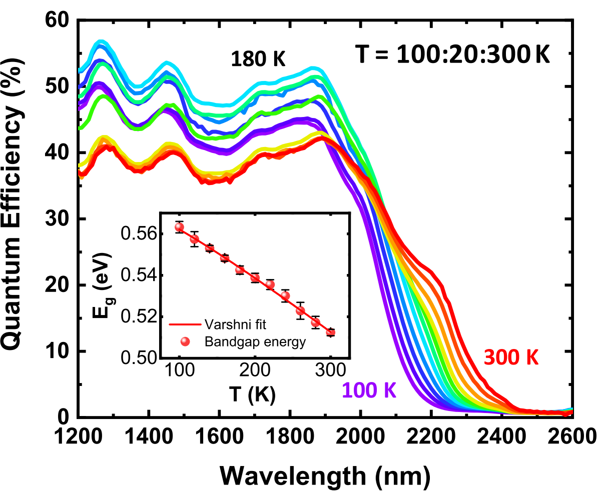

Fig. 4. Measured quantum efficiency spectrum of the photon-trapping photodetector at various temperatures. The inset shows the calculated bandgap energies from cut-off wavelengths at various temperatures with a line fitted to the Varshni expression.

The first one is a conventional reference photodetector with a bare surface and no reflective metal at the bottom. The second is a bonded reference photodetector, also with a bare surface, but incorporating reflective metal at the bottom through wafer bonding. The comparison with the bonded reference photodetector aims to determine whether the observed increase in quantum efficiency in the photon-trapping photodetector is solely due to the presence of the bottom reflective metal.

Figure 5 presents the comparison between the experimental and simulated quantum efficiencies of the conventional reference photodetector, the bonded reference photodetector, and the photon-trapping photodetector at 200 K. The measured average quantum efficiency of the conventional reference photodetector in the extended SWIR region, spanning from 1.7 µm to 2.5 µm, is 14.5%. In the same wavelength range, the bonded reference photodetector and the photon-trapping photodetector exhibit average quantum efficiencies of 17.5% and 25.7%, respectively.

The spectral quantum efficiency of the bonded reference photodetector displays periodic oscillations, with increases and decreases in quantum efficiency as the wavelength changes, which is attributed to vertical Fabry-Perot resonances induced by the bottom reflective metal. In contrast, the photon-trapping photodetector, despite also having a bottom reflective metal, shows an increase in quantum efficiency across all wavelengths. This enhancement is due to the diffraction grating, which induces multiple guided-mode resonances within the active layers. As a result, the photon-trapping photodetector achieves a significant average quantum efficiency improvement of 77.2% relative to the conventional reference photodetector, while the bonded reference photodetector shows only a 20.7% increase. Further improvements can be achieved by integrating an anti-reflective design with the photon-trapping structure and optimizing them simultaneously.

Figure 5 also includes simulated spectral quantum efficiencies for all three devices. The general consistency between the experimental data and simulation results suggests that the device structures were precisely implemented. It is believed that the minor discrepancies between the measured and simulated values are likely due to inevitable fabrication variations.

We further investigated the electric field distributions using FDTD simulations to understand the mechanisms underlying the quantum efficiency enhancement in each photodetector. Figure 6(a) illustrates the electric field distribution within the active layers of the conventional reference

Optics EXPRESS

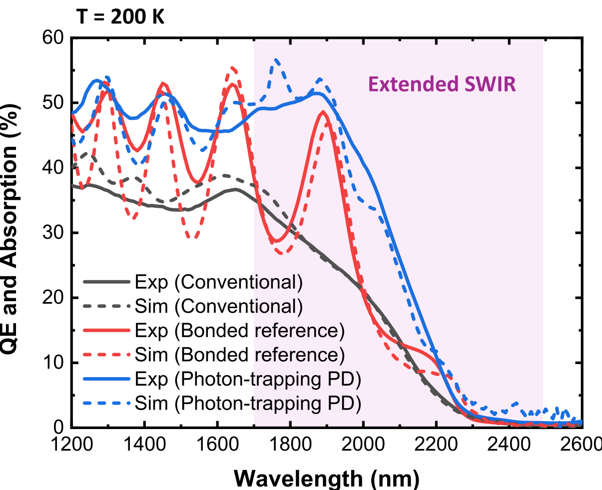

Fig. 5. Measured quantum efficiencies and simulated absorptions of the conventional reference photodetector, the bonded reference photodetector, and the photon-trapping photodetector. The extended SWIR region is colored.

photodetector at a wavelength of 2.34 µm. In this case, a weak Fabry-Perot resonance is observed, primarily due to the limited reflection of light at the interface with the GaSb substrate. However, a significant portion of the incident light is reflected from the surface rather than being absorbed by the active layer, resulting in suboptimal quantum efficiency.

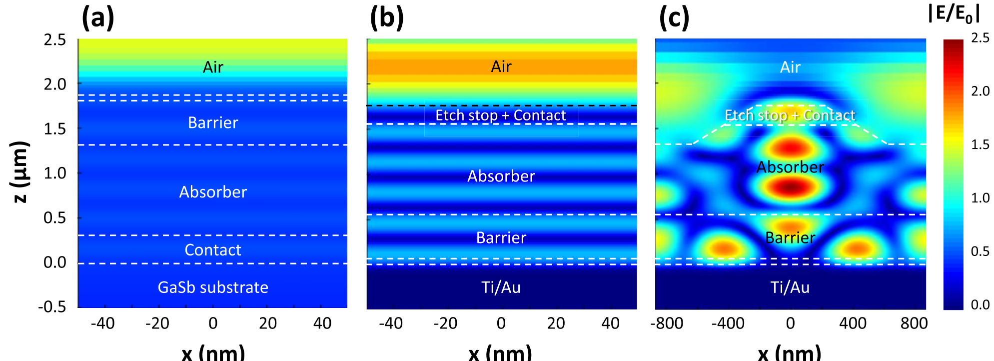

Fig. 6. Simulated electric field distributions of (a) the conventional reference photodetector, (b) the bonded reference photo-detector, and (c) the photon-trapping photodetector.

Figure 6(b) shows the electric field distribution for the bonded reference photodetector. Here, a strong Fabry-Perot resonance pattern is evident, attributed to the presence of the reflective metal beneath the active layer. This results in periodic oscillations in quantum efficiency as a function of wavelength.

In contrast, the photon-trapping photodetector exhibits a markedly different electric field distribution, as shown in Fig. 6(c). The diffraction grating effectively redirects vertically incident light to propagate laterally within the active layers. This lateral propagation substantially increases the effective optical path length, thereby leading to a significant enhancement in quantum efficiency. Unlike the other two photodetectors, where vertical Fabry-Perot resonances dominate, the photon-trapping structure benefits from the additional guided-mode resonances

Optics EXPRESS

induced by the diffraction grating, which contribute to the observed dramatic increase in quantum efficiency.

Finally, to gain deeper insight into the optical resonances present in the photodetector, we calculated the absorption as a function of both wavelength and grating period. Figure 7 illustrates the absorption distribution, revealing multiple optical resonances characterized by different mode numbers. Here, two distinct groups of optical resonances are observed.

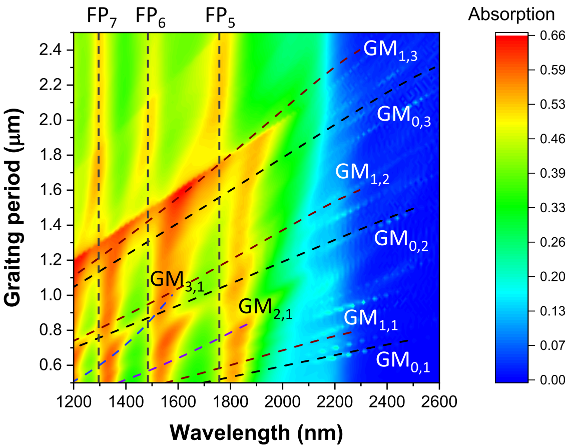

Fig. 7. Optical resonances with different mode orders indicated on absorption distribution by grating period and wavelength.

The first group consists of vertical Fabry-Perot resonances, indicated by vertical dashed lines at wavelengths of 1270 nm, 1480 nm, and 1770nm. These resonances are independent of the grating period, as they are solely induced by the bottom reflective metal. As noted in Fig. 1(c), these correspond to Fabry-Perot mode orders 7, 6, and 5, respectively.

The second group is represented by slanted lines, which are dependent on the grating period. These resonances are attributed to guided-mode resonances. When the diffracted light from the grating satisfies the guided-mode conditions of the waveguide, it propagates laterally along the waveguide, resulting in guided-mode resonance at the corresponding wavelength. To further understand these resonances, we theoretically calculated the guided-mode conditions using an asymmetric planar waveguide model and applied the diffraction grating equation to predict the resonance wavelengths [35,36]. First, the vertically incident light diffracts at the grating satisfies the condition given by

$$n_{\text{active}} \sin \theta(m) = -m \frac{\lambda}{\Lambda} \tag{2}$$

where n_{active} is the refractive index of active region, λ is the wavelength of the incident light, Λ is the grating period, and m is the diffraction order. Second, the guided-mode condition in an asymmetric planar waveguide is given by

$$-2k_z d + \phi_{21} + \phi_{23} = -2l\pi \tag{3}$$

here k_z is the vertical component wavevector in the active region, d is the thickness of the active region, ϕ_{21} and ϕ_{21} the phase change induced by reflection at the top and bottom interfaces of the active region, and l is the mode order. The guided-mode resonances with orders (l, m) were calculated using these equations and are indicated as $\text{GM}_{\text{l,m}}$ on the absorption distribution plot in Fig. 7. As depicted, the grating period-dependent absorption peaks generally align well with the theoretically calculated guided-mode resonances. This alignment confirms that the

Optics EXPRESS

overall enhancement in quantum efficiency observed in the photon-trapping structure results from the combined effects of both Fabry-Perot resonances and multiple guided-mode resonances. With these understandings, mode-ware device design will be possible depending on the specific targeted purpose.

5. Conclusion

In summary, we successfully enhanced the quantum efficiency of the eSWIR T2SL photodetector by implementing a photon-trapping structure comprising a diffraction grating and a reflective metal layer. The diffraction grating dimensions were carefully optimized using FDTD simulations, and the reflective metal was incorporated beneath the active region via wafer bonding. The diffraction grating diffracts incident light, causing it to propagate laterally within the active region of the photon-trapping photodetector, elongating the effective optical path length and thereby increasing absorption.

Optical measurements revealed that the photon-trapping photodetector achieved a 77.2% increase in average quantum efficiency compared to the conventional reference photodetector within the eSWIR range. Analyses of the electric field distribution and optical resonances support the conclusion that this improvement in quantum efficiency is attributable to the combined effects of Fabry-Perot resonances and multiple guided-mode resonances, induced by the synergy of the bottom reflective metal and the diffraction grating.

Funding. Ministry of Trade, Industry and Energy (20-CM-EO-07); National Research Foundation of Korea (2020M3H4A3081735, RS-2024-00416583).

Disclosures. The authors declare no conflicts of interest.

Data availability. Data underlying the results presented in this paper are not publicly available at this time but may be obtained from the authors upon reasonable request.

References

1. M. Razeghi, "9 - InAs/GaSb type II superlattices: A developing material system for third generation of IR imaging," in *Mid-Infrared Optoelectronics*, E. Tournié and L. Cerutti, eds., Woodhead Publishing Series in Electronic and Optical Materials (Woodhead Publishing, 2020), pp. 379–413.
2. R. Breiter, M. Benecke, D. Eich, *et al.*, "Extended SWIR imaging for targeting and reconnaissance," in *Infrared Technology and Applications XLIV* (SPIE, 2018), Vol. 10624, pp. 11–21.
3. G. A. Tidhar and R. Segal, "New applications with a SWIR imager employing extended wavelengths," in *Infrared Technology and Applications XXXVII* (SPIE, 2011), Vol. 8012, pp. 70–82.
4. D. Wei, A. A. Dadey, J. A. McArthur, *et al.*, "Enhancing Extended SWIR Al0.3InAsSb PIN Photodetectors with All-Dielectric Amorphous Germanium Photon-Capturing Gratings," ACS Photonics **11**(2), 484–488 (2024).
5. Y. Arslan, F. Oguz, and C. Besikci, "Extended wavelength SWIR InGaAs focal plane array: Characteristics and limitations," Infrared Phys. Technol. **70**, 134–137 (2015).
6. H. Yuan, J. Zhang, J. Kim, *et al.*, "Recent progress in extended wavelength InGaAs photodetectors and comparison with SWIR HgCdTe photodetectors," in *Infrared Sensors, Devices, and Applications IX* (SPIE, 2019), Vol. 11129, pp. 97–106.
7. A. Wörl, R. Müller, V. Daumer, *et al.*, "Investigation of InGaAsSb-based heterojunction photodiodes for extended SWIR imaging," in *Electro-Optical and Infrared Systems: Technology and Applications XX* (SPIE, 2023), Vol. 12737, pp. 36–39.
8. A. Dehzangi, R. McClintock, A. Haddadi, *et al.*, "Type–II superlattices base visible/extended short–wavelength infrared photodetectors with a bandstructure–engineered photo–generated carrier extractor," Sci. Rep. **9**(1), 5003 (2019).
9. G. Cao, T. Li, H. Tang, *et al.*, "Performance of extended wavelength InGaAs/InAsP SWIR detector," in *7th International Symposium on Advanced Optical Manufacturing and Testing Technologies: Optoelectronics Materials and Devices for Sensing and Imaging* (SPIE, 2014), Vol. 9284, pp. 30–37.
10. I. Shafir, D. Cohen-Elias, N. Snapi, *et al.*, "Improved performances InAs/AlSb Type-II superlattice photodiodes for eSWIR with Ldiff of 2.4 µm and QE of 38% at 300 K," Infrared Phys. Technol. **105**, 103210 (2020).
11. A. Kamboj, L. Nordin, A. J. Muhowski, *et al.*, "Room-Temperature Mid-Wave Infrared Guided-Mode Resonance Detectors," IEEE Photon. Technol. Lett. **34**(11), 615–618 (2022).
12. A. Rogalski, P. Martyniuk, and M. Kopytko, "Type-II superlattice photodetectors versus HgCdTe photodiodes," Prog. Quantum Electron. **68**, 100228 (2019).
13. Z. Xie, Z. Deng, X. Zou, *et al.*, "InP-Based Near Infrared/Extended-Short Wave Infrared Dual-Band Photodetector," IEEE Photonics Technol. Lett. **32**(16), 1003–1006 (2020).

14. S.-Y. Ko, B. W. Lee, H. J. Kim, *et al.*, “Comparison of InGaAs and type-II superlattice based extended SWIR detectors,” in *Infrared Technology and Applications XLVIII* (SPIE, 2022), Vol. 12107, p. 1210703.
15. A. Rogalski, “Infrared detectors: an overview,” Infrared Phys. Technol. **43**(3-5), 187–210 (2002).
16. N. D. Akhavan, G. A. Umana-Membreno, R. Gu, *et al.*, “Design Principles for High QE HgCdTe Infrared Photodetectors for eSWIR Applications,” J. Electron. Mater. **51**(9), 4742–4751 (2022).
17. A. Singh and R. Pal, “Performance of InGaAs short wave infrared avalanche photodetector for low flux imaging,” Appl. Phys. A **123**(11), 701 (2017).
18. D. Cohen-Elias, N. Snapi, O. Klin, *et al.*, “Minority carrier diffusion length for electrons in an extended SWIR InAs/AlSb type-II superlattice photodiode,” Appl. Phys. Lett. **111**(20), 201106 (2017).
19. D. Chen, S. D. March, A. H. Jones, *et al.*, “Photon-trapping-enhanced avalanche photodiodes for mid-infrared applications,” Nat. Photon. **17**, 594–600 (2023).
20. H. Dou, L. Liu, J. Gou, *et al.*, “Enhanced Response of Si-Based PbSe Thin Film MSM Photodetectors by Photon-Trapping Hole Array in the Surface,” ACS Photonics **11**(9), 3688–3696 (2024).
21. Y. Gao, H. Cansizoglu, K. G. Polat, *et al.*, “Photon-trapping microstructures enable high-speed high-efficiency silicon photodiodes,” Nat. Photonics **11**(5), 301–308 (2017).
22. H. Zhou, S. Xu, Y. Lin, *et al.*, “High-efficiency GeSn/Ge multiple-quantum-well photodetectors with photon-trapping microstructures operating at 2 µm,” Opt. Express **28**(7), 10280–10293 (2020).
23. W. Qarony, A. S. Mayet, E. Ponizovskaya-Devine, *et al.*, “Achieving higher photoabsorption than group III-V semiconductors in ultrafast thin silicon photodetectors with integrated photon-trapping surface structures,” Adv. Photon. Nexus **2**(5), 056001 (2023).
24. A. Y. Zhu, S. Zhu, and G.-Q. Lo, “Guided mode resonance enabled ultra-compact Germanium photodetector for 1.55 µm detection,” Opt. Express **22**(3), 2247–2258 (2014).
25. X. Cui, K. Tawa, K. Kintaka, *et al.*, “Enhanced Fluorescence Microscopic Imaging by Plasmonic Nanostructures: From a 1D Grating to a 2D Nanohole Array,” Adv. Funct. Mater. **20**(6), 945–950 (2010).
26. M. Alexe and U. Gösele, *Wafer Bonding: Applications and Technology* (Springer Science & Business Media, 2013).
27. R. Chevallier, A. Dehzangi, A. Haddadii, *et al.*, “Type-II superlattice-based extended short-wavelength infrared focal plane array with an AlAsSb/GaSb superlattice etch-stop layer to allow near-visible light detection,” Opt. Lett. **42**(21), 4299–4302 (2017).
28. A. Haddadi, R. Chevallier, A. Dehzangi, *et al.*, “Extended short-wavelength infrared nBn photodetectors based on type-II InAs/AlSb/GaSb superlattices with an AlAsSb/GaSb superlattice barrier,” Appl. Phys. Lett. **110**(10), 101104 (2017).
29. A. Dehzangi, A. Haddadi, R. Chevallier, *et al.*, “nBn extended short-wavelength infrared focal plane array,” Opt. Lett. **43**(3), 591–594 (2018).
30. D. Z. Ting, A. Soibel, A. Khoshakhlagh, *et al.*, “Antimonide e-SWIR, MWIR, and LWIR barrier infrared detector and focal plane array development,” in *Infrared Technology and Applications XLIV* (SPIE, 2018), Vol. 10624, pp. 110–117.
31. M. Bouschet, V. Arounassalame, A. Ramiandrasoa, *et al.*, “Temperature Dependence Study of Electrical and Electro-Optical Performances of Midwave Infrared Ga-Free T2SL Barrier Photodetector,” Appl. Sci. **12**(20), 10358 (2022).
32. D. Z. Ting, A. Soibel, A. Khoshakhlagh, *et al.*, “Mid-wavelength high operating temperature barrier infrared detector and focal plane array,” Appl. Phys. Lett. **113**(2), 021101 (2018).
33. H. Ünlü, “A thermodynamic model for determining pressure and temperature effects on the bandgap energies and other properties of some semiconductors,” Solid-State Electron. **35**(9), 1343–1352 (1992).
34. P. K. Sarswat and M. L. Free, “A study of energy band gap versus temperature for Cu2ZnSnS4 thin films,” Phys. B **407**(1), 108–111 (2012).
35. P. Yeh and M. Hendry, “Optical Waves in Layered Media,” Phys. Today **43**(1), 77–78 (1990).
36. E. G. Loewen and E. Popov, *Diffraction Gratings and Applications* (CRC Press, 2017).

114.70.7.207 2026-03-24 04:12:18